Numerical study of three-dimensional flows around two identical square cylinders in staggered arrangements

Jianlei Niu and Zuojin Zhu

Related Articles

Three-dimensional fit-to-flow microfluidic assembly
Biomicrofluidics 5, 046505 (2011)

Pumping of dielectric liquids using non-uniform-field induced electrohydrodynamic flow
Appl. Phys. Lett. 99, 224102 (2011)

Scaffold fabrication in a perfusion culture microchamber array chip by O2 plasma bonding of poly(dimethylsiloxane) protected by a physical mask
Biomicrofluidics 5, 022204 (2011)

Analytical solution on Magnus wind turbine power performance based on the blade element momentum theory
J. Renewable Sustainable Energy 3, 033104 (2011)

Retreat behavior of a charged droplet for electrohydrodynamic inkjet printing
Appl. Phys. Lett. 98, 083501 (2011)

Additional information on Phys. Fluids

Journal Homepage: http://pof.aip.org/

Journal Information: http://pof.aip.org/about/about_the_journal

Top downloads: http://pof.aip.org/features/most_downloaded

Information for Authors: http://pof.aip.org/authors

Numerical study of three-dimensional flows around two identical square cylinders in staggered arrangements

Jianlei Niu[a)]
*Department of Building Services Engineering, The Hong Kong Polytechnic University, Kowloon,
Hong Kong, People's Republic of China*

Zuojin Zhu[b)]
Department of Thermal Science and Energy Engineering, USTC, Hefei 230026, People's Republic of China

With the aim to understand air pollutant dispersion among high-density, high-rise buildings, this paper presents the numerical results of three-dimensional flows around two identical square cylinders (TISCs) in staggered arrangements at a Reynolds number of 250 and zero incident angle when the angle between the incoming velocity vector and the line connecting the centers of the cylinders is 45°. The dependence of the drag and lift, their root mean square values, and the Strouhal number on the horizontal spacing have been evaluated. It was found that the correlation coefficients between the drag and lift of the upstream square cylinder (SC-I) were close to unity, with those for the downstream square cylinder (SC-II) exhibiting a wavy form along the spanwise direction. The wavelength and the magnitude are closely related to the cylinder spacing. Secondary vortex coherent structures as well as the primary vortex structures were reported and discussed. © *2006 American Institute of Physics*. [DOI: 10.1063/1.2194077]

I. INTRODUCTION

Flows around two identical square cylinders (TISCs) are idealized representation of airflows around buildings and many other engineering structures. Flows encountered around buildings can vary from low Re number creeping flows to fully developed turbulent flows, depending on wind conditions. The study of the TISC flow at low Reynolds number conditions is related to the understanding of the dispersion of indoor air pollutants, and particularly pathogen-laden aerosols around high-density, high-rise buildings, as witnessed in the recent SARS outbreak.[1] Owing to the effect of the gap flow between the two square cylinders, the near-wake interference, and the possible far-wake emergence, certain important flow characteristics need to be explored. However, the corresponding numerical work remains scarce, while more recent studies were conducted on circular cylinder flows, and most of them are experimental work.[2] It was reported that for the flow around two staggered identical circular cylinders in cross-flow, there exist nine patterns when the center-to-center pitch ratio varies from 1 to 5, and the angle of incident changes from zero to 90°, with Reynolds number ranging from 850 to 1900. It was suggested that the vortex shedding frequencies are more properly associated with individual shear layers rather than with individual circular cylinders; more specifically, the two shear layers from the downstream cylinder often shed vortices at different frequencies.

The presence of gap flow effects results in complicated patterns of multiple cylinders flow, not only in the primary flow but also in the secondary flows when the Re is beyond the critical transitional value. Therefore, the spacing between the cylinders and the orientation relative to the freestream are dominant features that affect the flow interference, which might lead to the ineffectiveness for most methods used in suppressing the vortex shedding from multiple cylinders.[3–6] The spacing effect on the multicylinder wake flow has been measured and reported extensively,[7–10] but the relevant situation is either for side-by-side or tandem cylinder arrangement. Furthermore, in most of these studies[3–10] the association of the vortex shedding with the individual shear layers has not been well distinguished. In addition, it is possible for the two shear layers to shed vortices at different frequencies, but the cause of the different vortex shedding modes still requires further exploration.

In this paper, we focus on the numerical investigation of the flow past two identical square cylinders at a Reynolds number of 250. The purpose is to examine the influence of the cylinder spacing on the flow-induced forces and vortex shedding frequencies, and the effect of the primary wake interference on the secondary flow structures.

II. GOVERNING EQUATIONS AND NUMERICAL METHOD

A. Governing equations

For the wake flow around TISCs, as schematically shown in Fig. 1, it is convenient to present equations in nondimensional variables. Choose the units

$$[L] = d, \quad [T] = d/u_{\text{in}}, \tag{1}$$

where u_{in} is the oncoming flow velocity, and d is the side length of the square cylinder. The Reynolds number of the problem considered is $\text{Re} = du_{\text{in}}/\nu$, with ν being the kinematic viscosity of the fluid. The governing equation in a

---

[a)]Electronic mail: Bejlniu@polyu.edu.hk
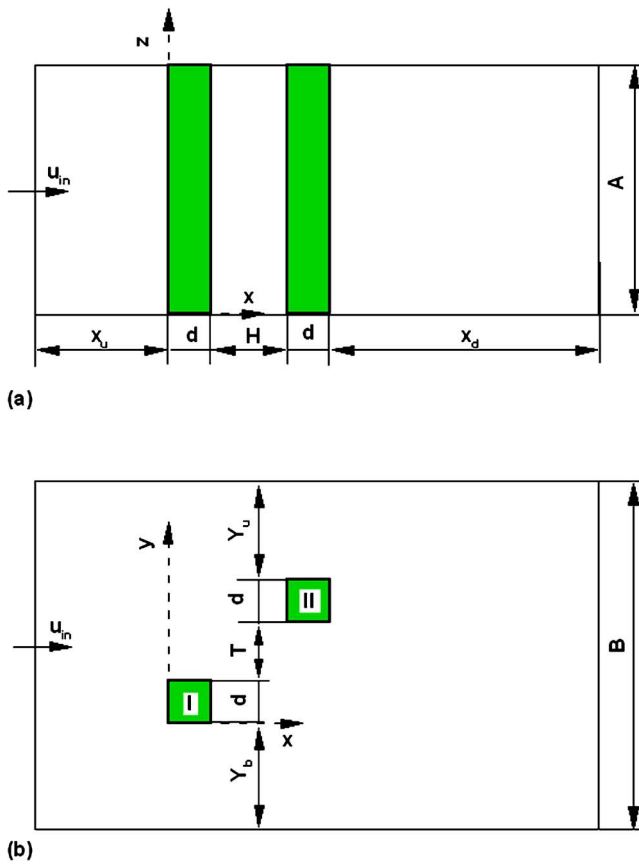[b)]Electronic mail: zuojin@ustc.edu.cn

FIG. 1. Schematic of flow past two identical square cylinders in stagger arrangement: (a) side view and (b) top view.

three-dimensional (3D) Cartesian coordinate system (x, y) can be written as the incompressible Navier-Stokes equations:

$$u_x + v_y + w_z = 0, \tag{2}$$

$$u_t + uu_x + vu_y + wu_z = -p_x + \nabla^2 u / \text{Re}, \tag{3}$$

$$v_t + uv_x + vv_y + wv_z = -p_y + \nabla^2 v / \text{Re}, \tag{4}$$

$$w_t + uw_x + vw_y + ww_z = -p_z + \nabla^2 w / \text{Re}, \tag{5}$$

whose vector forms are

$$\nabla \cdot \mathbf{u} = 0, \tag{6}$$

$$\mathbf{u}_t + (\mathbf{u} \cdot \nabla)\mathbf{u} = -\nabla p + \nabla^2 \mathbf{u} / \text{Re}. \tag{7}$$

The solutions of the governing equations (6) and (7) should be sought under appropriate boundary and initial conditions. For the boundary conditions (BCs) on the square cylinder walls, nonslip BC is used, which means that

$$u = 0, \quad v = 0, \quad w = 0, \tag{8}$$

while for the BC at the outlet, similar to the treatment utilized by Sohankar et al.[11] and Saha et al.,[12] we use the Orlanski[13] type

$$u_t + u_c u_x = 0, \quad v_t + u_c v_x = 0, \quad w_t + u_c w_x = 0. \tag{9}$$

In regard to the nondimensional form, we choose $u_c = 1$. At the inlet section, we have

$$u = 1, \quad v = 0, \quad w = 0. \tag{10}$$

However, on the lower and upper side boundaries of the computational domain, we use

$$u_y = 0, \quad v = 0, \quad w = 0. \tag{11}$$

The initial condition is given by

$$u = 1, \quad v = 0, \quad w = 0. \tag{12}$$

The periodical condition is used on the spanwise boundaries. Such periodical condition can be simply expressed as

$$\mathbf{u}(x, y, z, t) = \mathbf{u}(x, y, z + A, t), \tag{13}$$

where A is the depth of the computation domain as given in Fig. 1(a).

B. Numerical method

The solutions for the 3D unsteady Navier-Stokes equations were sought by using the accurate projection algorithm PmIII developed by Brown et al.,[14] with a nonuniform stagger grid. The intermediate velocity components were calculated excluding the pressure gradient terms. The corresponding pressure Poisson's equation was solved by the approximate factorization one (AF1) scheme[15] at first, and then by the stabilized biconjugate gradient method (Bi-CGSTAB) given by Von der Vorst[16] to improve the solution accuracy. The convective terms in the governing equations are spatially discretized by the third order upwind finite difference scheme, with the viscous diffusion terms by the second-order central difference scheme.

The computational convergence criterion for pressure iteration was chosen as the grid-number averaged global residual as low as 3.0×10^{-8}. The advantage of this joint iteration method is it has higher accuracy than those obtained by the AF1 method alone. The Bi-CGSTAB has been used alone for the pressure field prediction (Yang et al.[17]). However, many more steps are needed to obtain the pressure field. In the Bi-CGSTAB method, for the convenience of code construction, Jacobian-type preconditioner was used, since the symmetric successive overrelaxation (SSOR)-type preconditioner as given by Pennacchio and Simoncini[18] is more complex in coding, even though it was reported that the SSOR-type preconditioner has the best performance of solution convergence.

To detail the finite difference scheme, we take the process of discretization for the term uu_x in Eq. (3) as a special example. Assume the velocity component (u_{ijk}) is located at $(x_{i-1/2}, y_j, z_k)$ the standard point (x_i, y_j, z_k), α_i $(i = 1, 4)$ are the finite difference coefficients that can be derived from Taylor expansion, then, for the case of positive velocity component $u_{ijk} > 0$, the third-order upwind scheme can be expressed as
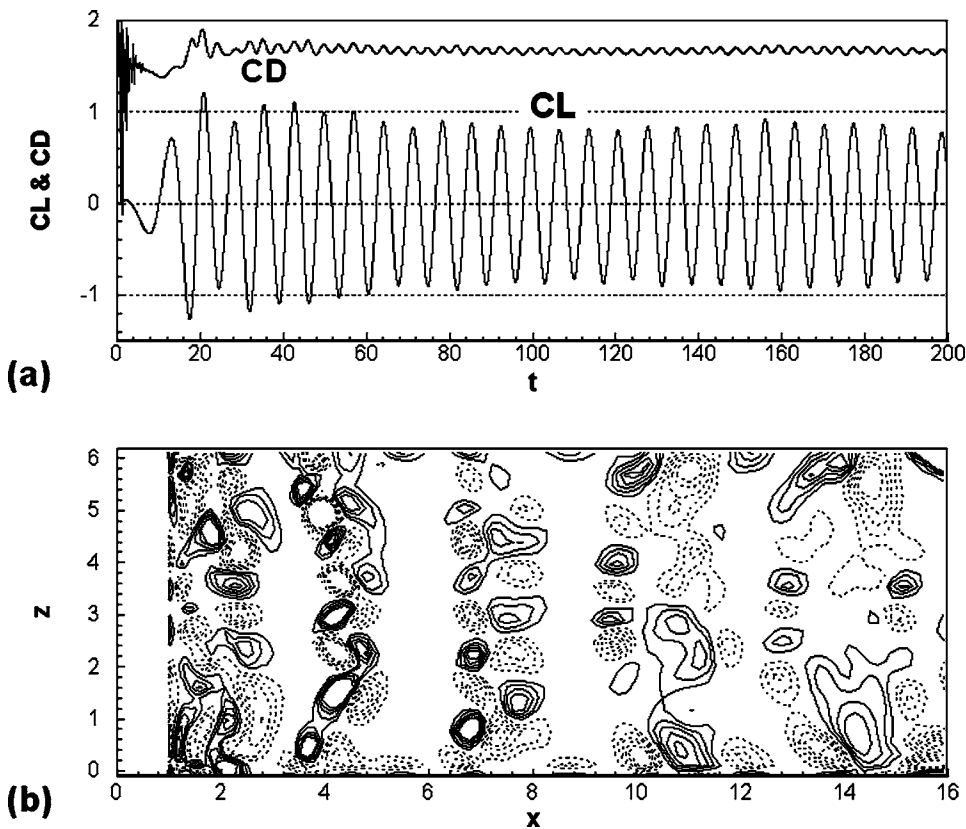
$$(uu_x)_{ijk} = u_{ijk}[-(\alpha_1 + \alpha_2 + \alpha_3)u_{ijk} + \alpha_1 u_{i-1,jk} + \alpha_2 u_{i-2,jk}$$
$$+ \alpha_3 u_{i+1,jk}] - \alpha_4 u_{ijk}(u_{xxxx})_{ijk}. \qquad (14)$$

Expressing $h_i = x_{i-1/2} - x_{i-1/2-1}$, according to the Taylor expansion of the velocities at point $(i-1, j, k)$, $(i-2, j, k)$, and $(i+1, j, k)$, we have the following coefficients of the scheme

$$\alpha_2 = \frac{s_3^3 + s_3^2}{h_i\Delta}, \quad \alpha_3 = -\frac{s_2^2 - s_2^3}{h_i\Delta}, \quad \alpha_1 = -\alpha_2 s_2^2 - \alpha_3 s_3^2, \qquad (15)$$

$$\alpha_4 = \begin{cases} [\alpha_1 h_i^4 + \alpha_2(h_i + h_{i-1})^4 + \alpha_3 h_{i+1}^4]/24, & \text{for } u_{ijk} > 0, \\ 0, & \text{otherwise,} \end{cases}$$
$$\qquad (16)$$

where $s_2 = (h_{i-1} + h_i)/h_i$, $s_3 = h_{i+1}/h_i$, and $\Delta = s_2 s_3(s_2 - 1)(s_3 + 1)(s_2 + s_3)$. The upwind scheme expressed by Eq. (14) has at least a third-order accuracy in discretization, since the coefficients $\alpha_i (i = 1, 2, 3)$ have the order of $O(1/h_i)$. Similar expressions can be derived for the upwind differencing of other convective terms in the momentum equations (3)–(5). It is noted that the fourth-order derivative of u can be discretized by the central difference approach, which is used for treating the diffusion terms in the governing equations. The overall solution procedure has been reported elsewhere,[19] with the main difference occurred in the discretization of the convective terms.

The numerical method was first assessed by comparing the St number and the time averaged drag for the single square cylinder flow with published results in 3D simulation reported by Sohankar et al.[11] and Okajima.[20] Using the grid $191 \times 131 \times 31$ and time step 0.004, the present method has

predicted that St and drag are 0.144 and 1.66, respectively, as shown in Fig. 2(a), for the single cylinder flow at Re=250 with a blockage of 5.6%. The measured St for this particular situation is about 0.142; the predicted St and drag by Sohankar, et al.[11] are, respectively, 0.158 and 1.43; with the values of 0.150 and 1.73 predicted by Saha et al.[12] in the situation of a blockage ratio 10%. As shown in Fig. 2(b), the secondary flow field at the instant of 200 for the single square cylinder flow at Re=250 has a vortical structure with a spanwise wavelength of about 1.2d, certainly containing small vortices. The comparison with experiment and the recent numerical results is satisfactory.

The computational domain for the flow past two square cylinders is shown in Figs. 1(a) and 1(b). The distance from the inlet section to the front side of the upstream SC denoted by x_u is set as 6.0, while the distance from the rear side of the downstream SC-II to the flow outlet section denoted by x_d is set as 15, with the values of y_b and y_u set as 8.5. Hence, the width of the computational domain B can be expressed as $(2d + T + y_b + y_u)$, the blockage of the flow in the present calculation can be expressed as $2d/B$, while the transverse spacing T is equal to longitudinal spacing H for the case of 45° of cylinder arrangement. The spanwise depth A is set as 11. In the simulation, the small mesh size near a SC sidewall is about 0.01, and the grids in the spanwise direction were uniform.

The grid independence inspection for the 3D flow simulation was carried out prior to extensive numerical simulation, for the case of $H = 1.0$. Using the grid $181 \times 155 \times 41$, the St number and the spanwise-averaged time-mean drag are, respectively, $St_{I1} = 0.118$, $St_{I2} = 0.255$, $St_{II} = 0.118$, CD_I
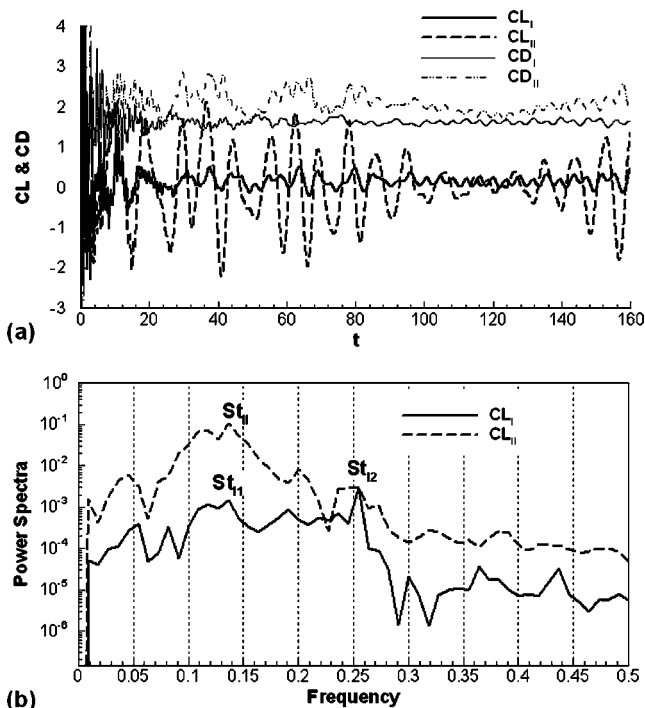
(a)

(b)

FIG. 3. (a) Evolution of the lift and drag coefficients for the flow past the TISC. (b) The diagram of power spectra for the evolution of lift coefficients on the TISC for the case of Re=250 and H=1. Note that the time has the unit of d/u_{in}, and the frequency has the unit of u_{in}/d. The two peaks of the solid curve are labeled with St_{I1} and St_{I2}, with the peak of the dashed curve labeled with St_{II}.

=1.631, and CD_{II}=2.070, with the relevant values St_{I1} =0.118, St_{I2}=0.247, St_{II}=0.118, CD_I=1.635, and CD_{II} =2.157 for the grid $181 \times 155 \times 26$. This means that the results are almost independent of the spanwise grid number. It

is noted that St_{I1} and St_{I2} are, respectively, the St numbers corresponding to the vortex shedding from inner and outer shear layers of upstream square cylinder (SC-I), while St_{II} is the St number relevant to the vortex shedding from the downstream square cylinder (SC-II). CD_I and CD_{II} represent the time-mean spanwise-averaged drag of cylinders SC-I and SC-II, respectively.

It is indicated that it is the upstream rather than the downstream cylinder that has duplicated frequencies of vortex shedding. This, however, is different from the visualization in staggered circular cylinder flows,[2] where it was found that the duplicated frequencies of vortex shedding occur on the downstream circular cylinder. Nevertheless, the power spectra for the lift on both square cylinders shown in Fig. 3(b) support that there are two St numbers for the vortex shedding from the upstream SC-I. The presence of the two St numbers at H=1.0 is likely caused by the particular staggered arrangement of the two identical square cylinders, which forms an oblique gap jet impinging in the near wake of the upstream SC-I; therefore, the flow in the inner shear layer of SC-I has to separate with a higher frequency than that separating in the outer shear layer of SC-I.

III. RESULTS AND DISCUSSION

The TISC flows were investigated numerically by solving the 3D incompressible unsteady Navier-Stokes equations, using the numerical approach presented in the foregoing sections. It was assumed that the transversal spacing T between the two identical SCs is the same as longitudinal spacing H, indicating that the angle between the incoming velocity vector and the line connecting the centers of the

TABLE I. Summary of results for the numerical simulation of flow around TISCs at Re=250. Note that H is the longitudinal spacing, CD and CL represent the time spanwise-averaged drag and lift, respectively, while CD′ and CL′ represent the spanwise-averaged rms of drag and lift. The subscript "I" refers to the SC-I, and "II" refers to the SC-II.

H	Grid	Δt	CD_I	CL_I	CD_I'	CD_I'	St_{I1}	St_{I2}
0.25	$181 \times 135 \times 41$	2.5×10^{-3}	2.173	−1.348	0.239	0.279	0.0819	0.0819
0.5	$181 \times 139 \times 41$	4×10^{-3}	1.834	−0.475	0.136	0.177	0.0819	0.0819
0.75	$181 \times 147 \times 41$	4×10^{-3}	1.677	−0.021	0.082	0.126	0.118	0.118
1.0	$181 \times 155 \times 41$	4×10^{-3}	1.631	0.155	0.061	0.126	0.137	0.255
1.25	$181 \times 161 \times 41$	4×10^{-3}	1.600	0.184	0.067	0.240	0.137	0.200
1.5	$181 \times 163 \times 41$	4×10^{-3}	1.616	0.132	0.066	0.324	0.137	0.182
2.0	$181 \times 163 \times 41$	4×10^{-3}	1.644	0.067	0.037	0.336	0.164	0.164
2.5	$181 \times 173 \times 41$	4×10^{-3}	1.667	0.042	0.045	0.409	0.155	0.155
3.0	$191 \times 183 \times 41$	4×10^{-3}	1.710	0.019	0.080	0.575	0.146	0.146

| H	Grid	Δt	CD_{II}	CL_{II}	CD_I'	CD_I'	St_{II}
0.25	$181 \times 135 \times 41$	2.5×10^{-3}	2.145	−0.109	0.245	0.600	0.0819
0.5	$181 \times 139 \times 41$	4×10^{-3}	2.061	−0.076	0.292	0.631	0.0819
0.75	$181 \times 147 \times 41$	4×10^{-3}	2.117	0.018	0.250	0.821	0.118
1.0	$181 \times 155 \times 41$	4×10^{-3}	2.070	0.014	0.219	0.725	0.137
1.25	$181 \times 161 \times 41$	4×10^{-3}	2.319	0.040	0.229	1.300	0.137
1.5	$181 \times 163 \times 41$	4×10^{-3}	2.291	0.011	0.255	1.339	0.137
2.0	$181 \times 163 \times 41$	4×10^{-3}	2.244	0.010	0.218	1.388	0.146
2.5	$181 \times 173 \times 41$	4×10^{-3}	2.165	−0.006	0.206	1.428	0.146
3.0	$191 \times 183 \times 41$	4×10^{-3}	2.095	0.017	0.205	1.415	0.146
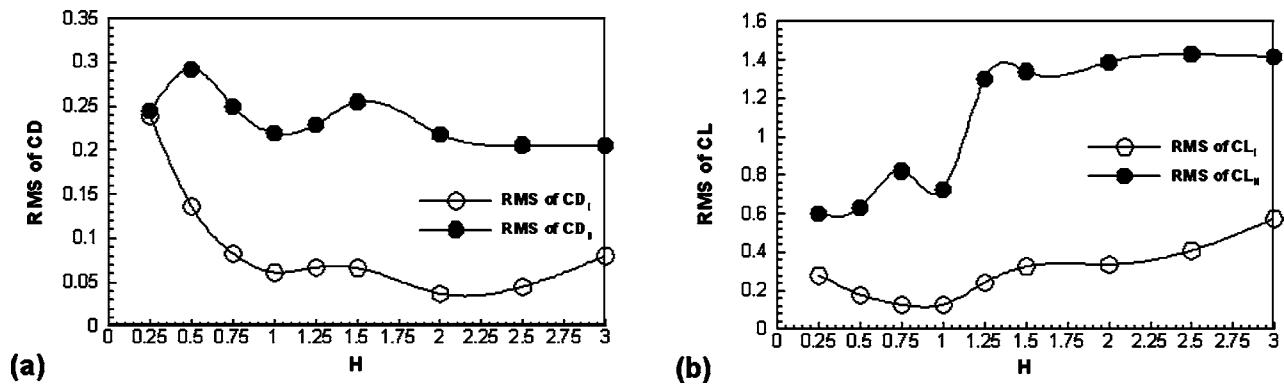
FIG. 4. (a) Spanwise-averaged drag and (b) lift as functions of longitudinal spacing H.

cylinders is 45°. The computation for the TISC flow at Re=250 was done on a PC with an internal memory of about 1 GB in two temporal stages, each containing around 20 000 time steps; the time step is generally 0.004, and the computation should be terminated at the instant $t=160$. For one case, the required CPU time is approximately 84.3 h. Nine cases of the TISC flows for different values of longitudinal spacing H were considered in this study, as seen in Table I.

The TISC flow at Re=250 involves the same vortex dynamical phenomena, such as vortex transition in mode A and mode B and the vortex dislocations in the secondary flow patterns. In addition, the vortex pairing, splitting, and enveloping (VPSE) flow patterns occurred in the spanwise vortex fields. Mode A would appear to be due to an elliptical instability of the primary vortex core during the process of shedding, which causes a spanwise waviness.[23] The deformation of the primary vortices in a wavy fashion results in the local spanwise formation of vortex loops, which become stretched into streamwise vortex pairs. The spanwise length scale of these vortex loops for single square cylinder flow is around $5.2d$ (Luo *et al.*[24]), with a value of $3d \sim 4d$ for the single circular cylinder flow.[23] It appears that the mode B structure is caused by an instability that scales on the thickness of the vorticity layer lying in the braid region. In the case of mode B, the primary vortex deformation is more spanwise-uniform than for mode A, and the streamwise vortex structure has a markedly smaller spanwise wavelength of around $1.2d$ for

single square cylinder flow,[24] with a value of about $1d$ for single circular cylinder flow.[23]

The vortex dislocations in the wake flow transition regimes are generated between spanwise cells of different frequency when the primary vortices move out of phase with each other. The dislocations are found to be generated at the sites of particular vortex loop, typical of mode A instability, and evolve spontaneously along the span, independent of the end conditions.[23] VPSE is a particular flow pattern found in the staggered circular cylinder flow, identified with respect to the primary vortex structures observed in the near wake.[2]

With the vortex dynamical phenomena briefly explained, the numerical results of this study will be presented and discussed in three parts: (a) drag, lift, and St, (b) spanwise correlation coefficients (SCCs) of the drag and lift, and (c) the flow fields.

A. Drag, lift, and St

For the flow around TISCs in a stagger arrangement, the combined effect of gap flow and wake flow interference renders the spacing H a primary dominant of time-mean spanwise-averaged drag and lift. Since the TISC is in staggered arrangement, as illustrated in Fig. 1, the gap flow, which is composed of the central jet and the two shear flow layers in the inner side of the TISC, transfers more momentum into the near wake of the upstream square cylinder
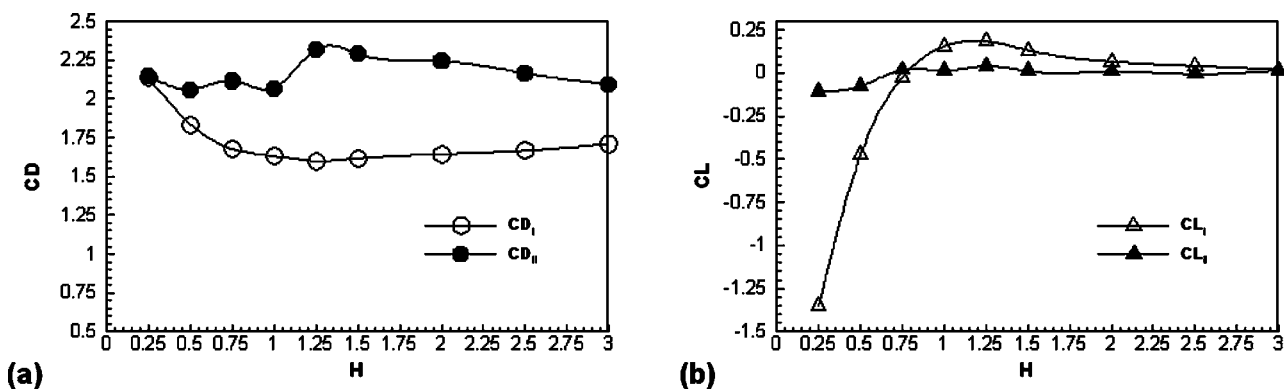

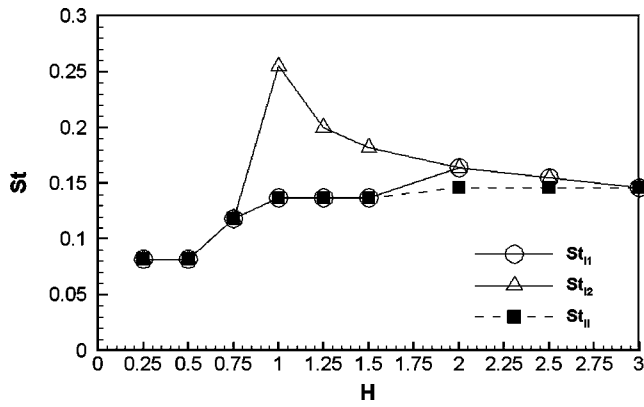FIG. 5. (a) Rms of spanwise-averaged drag and (b) lift as functions of longitudinal spacing H.

FIG. 6. Plot of St as a function of longitudinal spacing H. Note that the bifurcation of St_I indicates that there are two primary modes of vortex shedding on SC-I, the higher value of St_I is corresponding to the vortex shedding from the inner shear layer of SC-I, with the lower one relevant to vortex shedding from the outer shear layer of SC-I.

(SC-I), resulting in a comparatively small drag and lift on SC-I, as compared with those on the downstream square cylinder (SC-II), as given in Table I. It also affects the vortex shedding behaviors on both square cylinders. For some particular spacing values, the numerical results have confirmed the visualization-based indication that vortex shedding should be viewed as being from the different shear layers of the cylinders.[2]
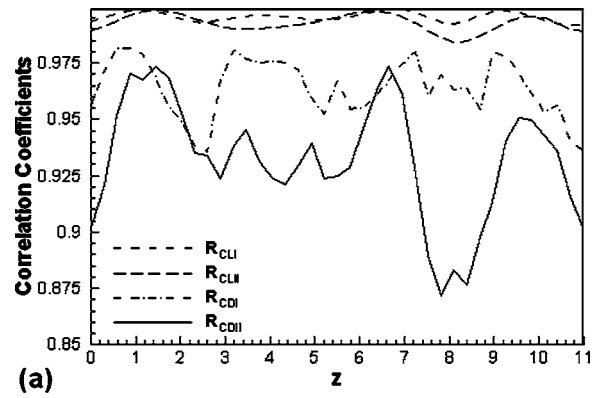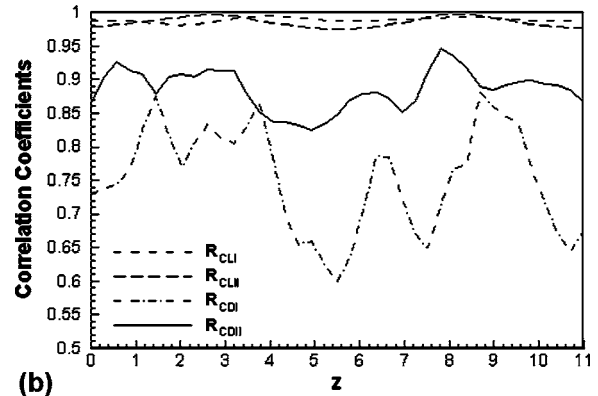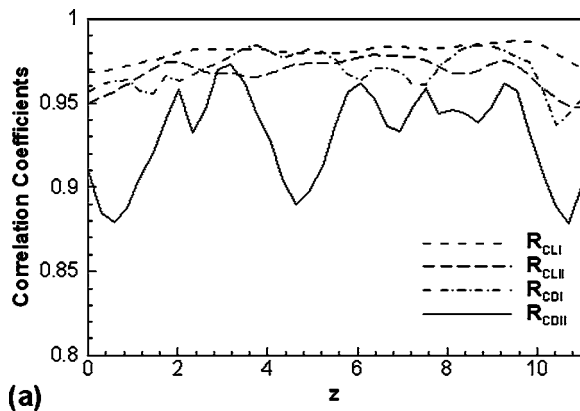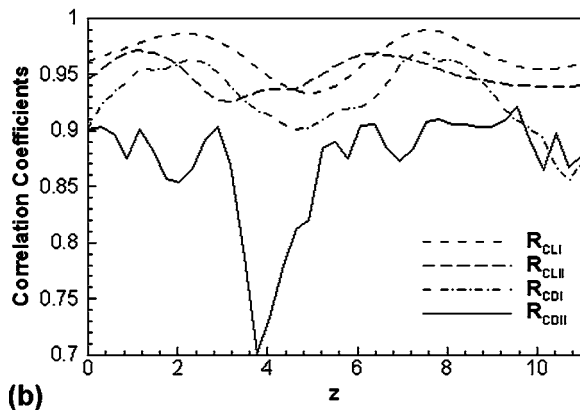

FIG. 8. Plot of spanwise correlation coefficients of drag and lift as a function of spanwise coordinate (z) for Re=250: (a) $H=1.5$ and (b) $H=2.0$.

Figure 3(a) shows the spanwise-averaged drag and lift for the TISC flow in staggered arrangement at Re=250 and spacing $H=1.0$, with Fig. 3(b) illustrating the corresponding power spectra based on the lift evolution and obtained by Hilbert transformation.[21] Mainly responsible for the impingement of the gap flow in the lower wake, the lift on SC-I oscillates in lower magnitudes and duplicates the main frequencies, suggesting that at this particular spacing ($H=1.0$) the vortex shedding from the inner and the outer shear layers of SC-I corresponds to duplicate St, denoted by St_{I1} and St_{I2}. According to the results of visualization for the flow around two identical circular cylinders, St_{I1} and St_{I2} should be, relevant to the vortex shedding from, respectively, the outer and inner shear layers of SC-I. However, for SC-II, there is only a single value of St number, since the value of the main peak in the lift power spectrum is much higher than that of the second peak located at a frequency of about 0.2, by approximately one order, as seen in Fig. 3(b).

Figures 4(a) and 4(b) show the time-mean spanwise-averaged drag and lift as functions of the longitudinal spacing. From Fig. 4(a), it is seen that the drag on SC-I is generally smaller than that on SC-II, except for the case of smallest spacing ($H=0.25$), for which the time-mean spanwise-averaged drag on SC-I (CD_I) is approximately identical to that on SC-II (CD_{II}). The curve of drag CD_I is smoother, compared with the curve of drag CD_{II}. The former has a valley and the latter has a peak at the spacing of about $H=1.25$, showing that there are two different trends of drag
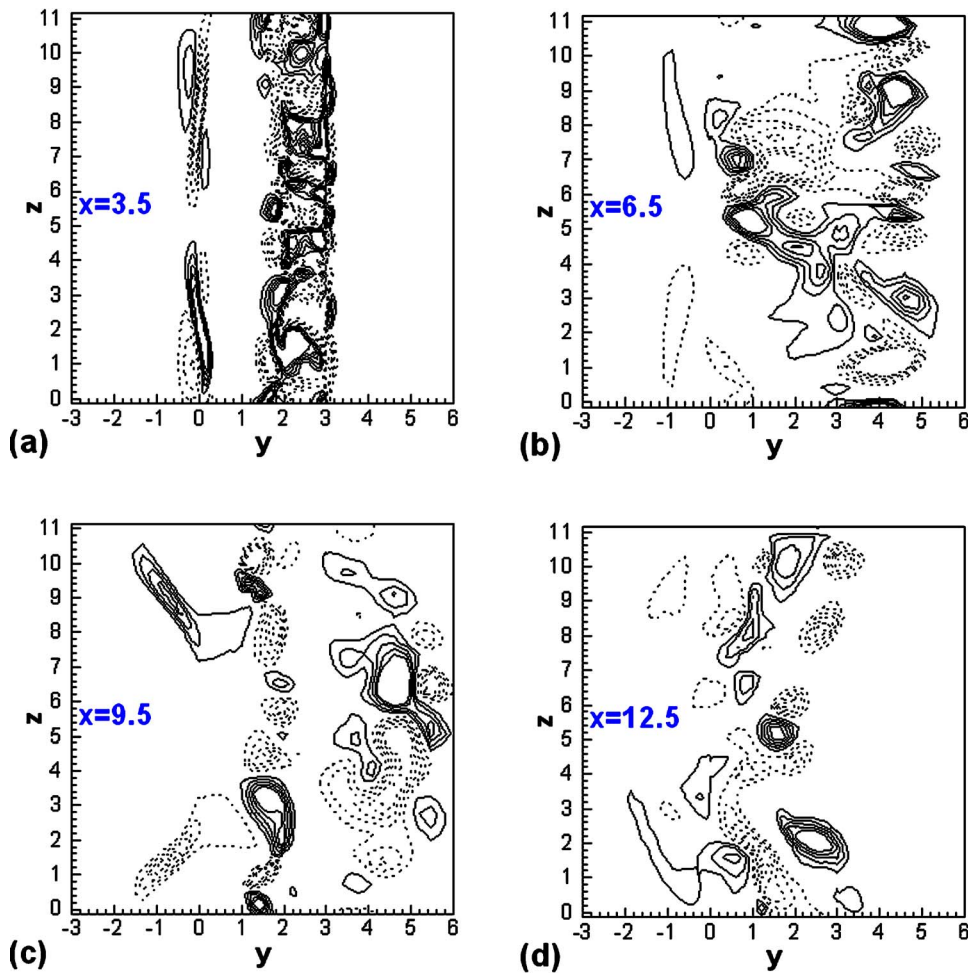

FIG. 7. Plot of spanwise correlation coefficients of drag and lift as a function of spanwise coordinate (z) for Re=250: (a) $H=0.5$ and (b) $H=1.0$.

FIG. 9. Contours of the vorticity component ω_x for the case of Re=250 and H=1 at the instant of t=80. These contours are shown, respectively, in four different secondary flow planes defined by x=3.5, 6.5, 9.5, and 12.5 in different parts from (a) to (d), the variation range and the increment of the vorticity component are given by $(\omega_{x\,min}, \omega_{x\,max}, \Delta\omega_x)=(-1,1,0.2)$, with the zero vorticity contour removed.

variation with the spacing. Clearly, the drag CD_{II} curve indicates a more sensitive response to the change of spacing.

As seen in Fig. 4(b), an evident repulsive transverse force on SC-I occurs due to the impacting of the gap flow, when the spacing is smaller than 0.75. For larger spacing, the wake interference might make the two cylinders mutually attracting. Such effect becomes more significant when the spacing is around 1.25. This to some extent can explain why ocean ships in motion should avoid navigating too closely.

Similarly, as evidently illustrated in Figs. 5(a) and 5(b), the values of the root mean square of the spanwise-averaged drag and lift on the SC-II are more sensitive to the cylinder spacing, and larger as compared with those relevant to SC-I. With the increase of spacing, both the curve of the rms of CD_I and the curve of the rms of CD_{II} are wavy, and the former has a local peak at the spacing of about 1.25, while the latter has both local peaks occur at the spacing of about H=0.5, and 1.5 [Fig. 5(a)]. As seen in Fig. 5(b), the values of the rms of CL_{II} are much larger than those of SC-I.

It is noted there are local valleys on the curves of CD_{II}, the rms of CD_{II}, and the rms of CL_{II} at the spacing of about 1.0, suggesting that at this particular spacing there are active wake interference and particular secondary flow structures. The observed dependences of drag and lift on the cylinder spacing suggesting that the gap flow and the wake interference certainly play dominating1 roles in the TISC flow.

On the other hand, the plotting of the St number of vortex shedding from SC-I as a function of spacing shows a bifurcation at certain spacing values, such bifurcation does not occur for the St of vortex shedding from SC-II (Fig. 6). Figure 6 suggests that the visualization-based conclusion of Sumner et al.[2] would be partially correct, since the St bifurcation merely appears at certain spacing. The present numerical results tend to conclude that it is the vortex shedding from the upstream cylinder rather from the downstream cylinder that has duplicated St numbers. Furthermore, because the St_{I1} relevant to the vortex shedding from the outer shear layer of SC-I is the same as that of the St for SC-II when the spacing is ranged from 0.25 to 2.0, this would mislead to a view that there is only one St for SC-I in the situations of the spacing ranged from 1.0 to 1.5. In addition, the difference between the numerical results and the visualization is likely to originate from the distinct vortex separation behaviors; for TISC flows, there are fixed separation points, while for staggered circular cylinder flow, the vortex separation from the cylinder wall has varying points.

B. Spanwise correlation coefficients

The spanwise correlation coefficients of drag and lift are signs of the presence of the secondary flow in the cross sec-
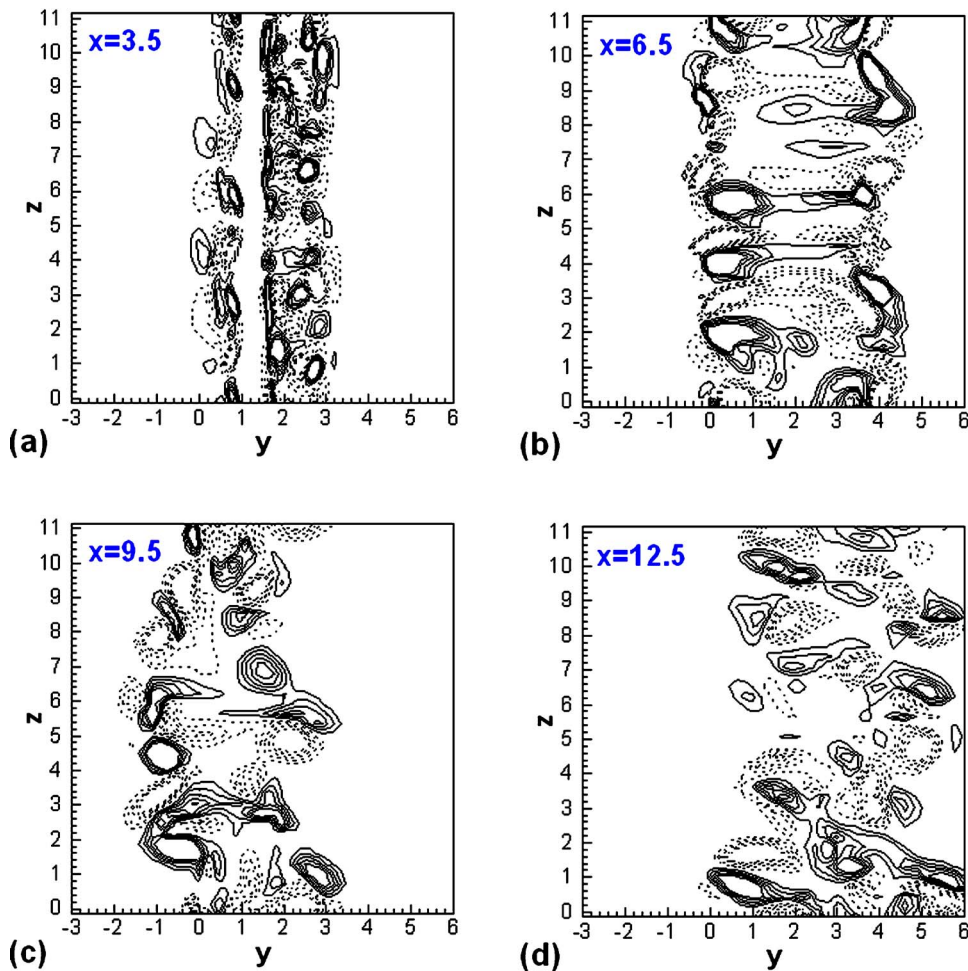
FIG. 10. Contours of the vorticity component ω_x for the case of Re $=250$ and $H=1$ at the instant of t $=160$. These contours are shown, respectively, in four different secondary flow planes defined by $x=3.5$, 6.5, 9.5, and 12.5 in different parts from (a) to (d), the variation range and the increment of the vorticity component are given by $(\omega_{x\,min}, \omega_{x\,max}, \Delta\omega_x)$ $=(-1,1,0.2)$, with the zero vorticity contour removed.

tion, indicating that in different vertical planes, the primary flow might be nonidentical. The evaluation method of the SCCs has been described in Ref. 22.

Figure 7(a) indicates that, for the spacing $H=0.5$, the SCC of drag and that of lift on SC-I have wavy distributions along the spanwise direction, and values are in the range from 0.94 to 0.98. Such small variations of the SCC values suggest that the secondary flow in the very near wake of SC-I is rather weak. However, the values of the SCC of lift on SC-II are slightly less than that on SC-I, with the largest difference around 0.02, while the SCC curve of drag on SC-II behaves as an apparent oscillation, with the largest magnitude of about 0.05. Since the SCC curve of drag can be viewed as a response to the joint effect of the primary vortices and the secondary organized vortices in the near wake region. But the oscillation of SCC curves is caused mainly by the secondary vortices in the near wakes of the two identical square cylinders. From the oscillation behavior of the SCC curves of drag, the mean spanwise wavelength of the secondary organized structures in the very near-wake zones can be evaluated approximately. As shown in Fig. 7(a), for the case of $H=0.5$, the mean wavelength of the secondary organized structures in the very near wake of the TISC flow is about $1.83d$. Similarly, for $H=1.0$, Fig. 7(b) suggests that the mean spanwise wavelength is $5.5d$ for the secondary organized structures in the very near wake of SC-I, with a value of $1.57d$ for that of the secondary organized structures

in the very near wake of SC-II. As illustrated in Fig. 8, the longitudinal spacing has a significant effect on the distributions of the SCC curves of drags and lifts of the TISC flow. For instance, the SCC curve of drag on SC-I is in general over that on SC-II as seen in Fig. 8(a), while reverse situation can be seen in Fig. 8(b). The mean spanwise wavelength of the secondary organized structures is $1.38d$ or $1.57d$, since the counted peak number of the SCC curves is about 7 or 8. The appearance of the wavy SCC curves indicates that the TISC flow at Re$=250$ does have its particular three dimensionality, which is closely related to the wake interference that affects primary vortex deformation rate.

C. Flow fields

In Figs. 9–16, unless otherwise noted, the flow fields are represented by vorticity contours, in which the dashed lines denote the contours having vorticity ranged from -1 to -0.2, and the solid lines denote the contours having vorticity ranged from 0.2 to 1, the vorticity increment is set as 0.2.

The secondary flow fields in four different cross sections for the case of spacing being equal to unity at time $t=80$ are shown in Fig. 9. Vortex dislocations can be found in Fig. 9. These dislocations appear at the sites of the mode A structure, as shown in Fig. 9(a) in the region at about $y=0$, the spanwise wavelength is around 5.2. This wavelength value is in good agreement with the visualization for single square
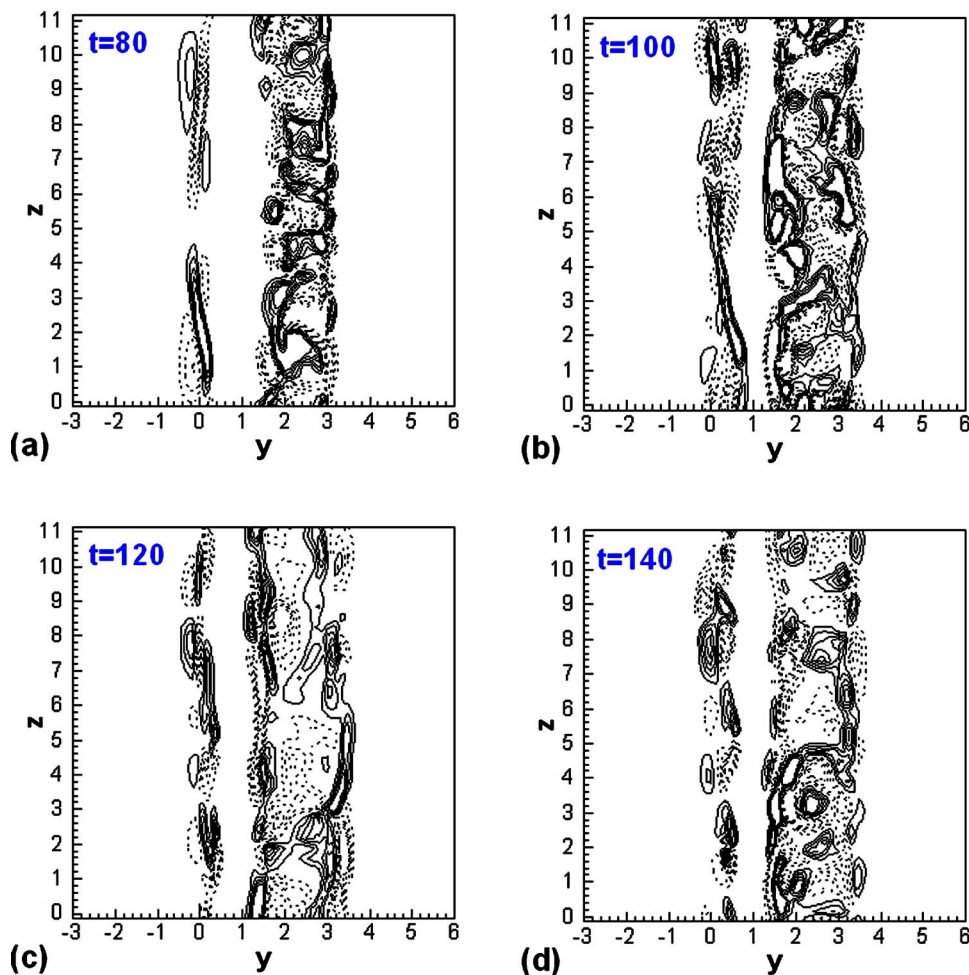
FIG. 11. Contours of the vorticity component ω_x for the case of Re $=250$ and $H=1$ at the plane $x=3.5$. These contours are shown, respectively, in four different instants defined by $t=80$, 100, 120, and 140 in different parts from (a) to (d), the variation range and the increment of the vorticity component are given by $(\omega_{x\,min}, \omega_{x\,max}, \Delta\omega_x)=(-1,1,0.2)$, with the zero vorticity contour removed.

cylinder flow at Re$=190$. However, the mode A structure occurred at the special instant of $t=80$. With the evolution of the secondary flow, the vortex stretching has resulted in a mode B structure at the instant of 160, as can be seen in Fig. 10(a).

An evident braid region is found in Fig. 9(a) at the sites around $y=2$. In this region, the secondary flow field is typically of mode B type, whose spanwise wavelength is about $1.2d$. At the instant of $t=80$, it can be seen that due to the suppressing effect of the gap flow, the secondary flow intensity in the near wake of SC-I is rather weak.

However, in the wake of SC-II, depending on the streamwise location, at which the primary vortex deforms in a different rate, and the way of wake interference is certainly different, there appears secondary vortex pairing, enveloping, and splitting phenomena. The vortex pairing and splitting promote the formation of the mode B structure, while the vortex enveloping leads to the occurrence of the mode A structure. Accordingly, the secondary flow fields shown in Fig. 9 can be seen as a mixture of mode A and B structures.

The coherent secondary flow structures in the same four cross-sections but at the instant of $t=160$ are given in Fig. 10. It is seen that in the section of $x=3.5$ [Fig. 10(a)] mode B prevails in both wakes of the TISC flow.

In Figs. 10(b) and 10(c), in the section of $x=6.5$, and 9.5, the vortex enveloping between the left and right braid re-

gions occurs, this implies that the primary vortex deforms at the situation of strong wake interference. The secondary vortex enveloped structures also occur in Fig. 10(d) in the section of $x=12.5$. In general, at the time of $t=160$, due to the comparatively fully developed secondary flow, there prevails mode B structures in the flow fields.

The comparison of Figs. 9 and 10 shows that the secondary flow field is certainly unsteady. Flow patterns change with time evolution. This certainty can be further observed in Figs. 11 and 12. Figure 11 depicts the secondary flow fields in the section of $x=3.5$ at four different instants, with Fig. 12 showing the flow fields in the section of $x=6.5$. It should be noted these temporal variation of secondary flow structures are closely connected with the primary flow in the constant-$z$plane as seen in Fig. 13(c), where the Karman vortex street can be seen. The secondary vortex enveloping in the braid region of Fig. 11 caused by wake interference can be seen as the reason that there is smaller lift oscillating magnitude during the time from $t=100$ to 130.

The contours of secondary vortices at the instant of $t=160$ are illustrated in Figs. 13(a) and 13(b), with part (c) showing the relevant primary wake flow pattern for the case of spacing being equal to unity. The secondary structures corresponding to $H=1$ were plotted in the mid planes of $y=0.5$, and 2.5. Evidently, the secondary flow fields are approximately symmetrical to the midplane of $z=6.0$. The in-
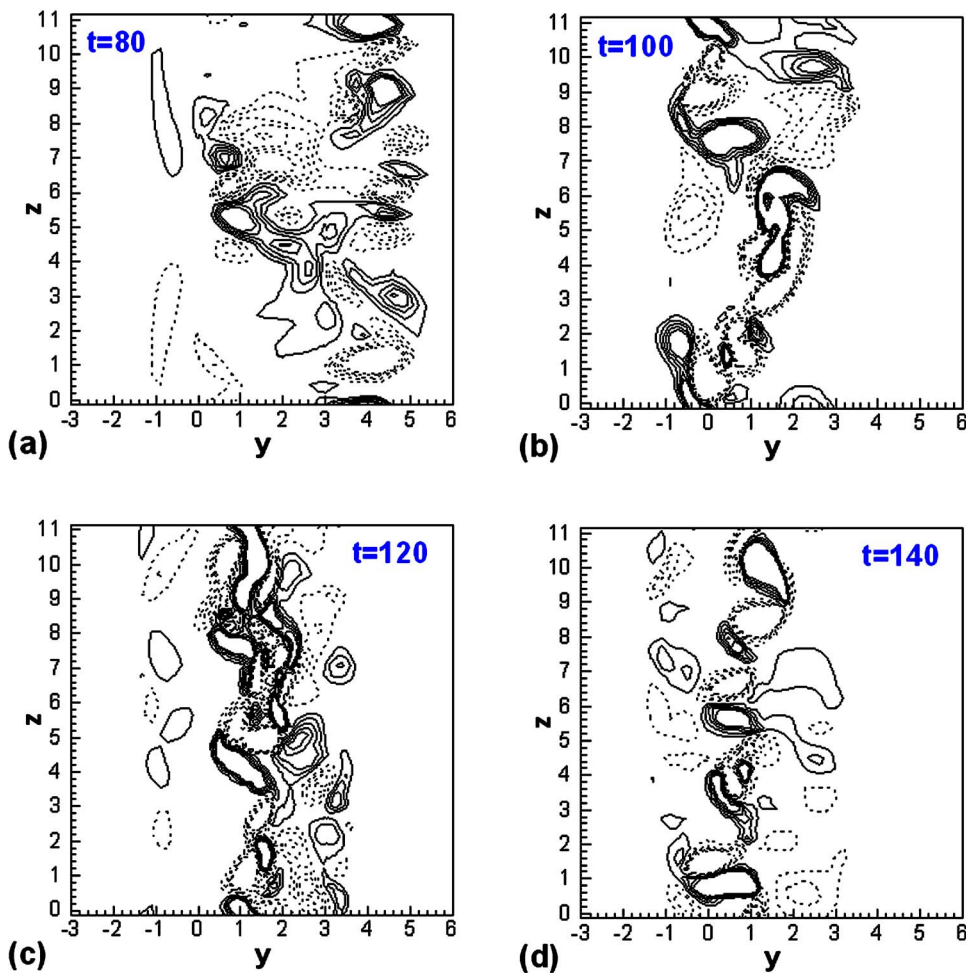
FIG. 12. Contours of the vorticity component ω_x for the case of Re $=250$ and $H=1$ at the plane $x=6.5$. These contours are shown, respectively, in four different instants defined by $t=80$, 100, 120, and 140 in different parts from (a) to (d), the variation range and the increment of the vorticity component are given by $(\omega_{x\,\min}, \omega_{x\,\max}, \Delta\omega_x) = (-1, 1, 0.2)$, with the zero vorticity contour removed.

tensity of vortices in the near wake of SC-I is very weak. In contrast, it is strong in the near wake of SC-II, where mode B structures prevail. This provides the reason of why the time-spanwise-averaged drag on SC-II is larger. This also indicates that the gap flow can suppress the generation of secondary vortices in the near wake of SC-I.

It is seen in Figs. 13(a) and 13(b) that the mode B does exist. However, this structure has been deformed and different from that observed in the single square cylinder wake [Fig. 2(b)]. There appears vortex enveloping due to wake interference, which results in a rather complicated coherent secondary flow pattern. This vortex enveloping causes the spanwise wavelength to become large, particularly in the far wake region.

However, the secondary flow fields in the constant y planes are sensitive to the spacing, as shown in Figs. 14(a) and 14(b) for the case of spacing of $H=2.0$. With the increase of spacing, the suppressing role of the gap flow becomes weak, the intensity of the secondary vortices in the near wake of SC-I become as large as those occurred in the near wake of SC-II. Figure 14(c) shows that there are two apparent wakes for the case of $H=2$; the wake interference is weaker than that in the case of $H=1$. As a result, the secondary vortex enveloping as shown in Figs. 14(a) and 14(b) is not as active as seen in Figs. 13(a) and 13(b). In addition, the

intensity of the secondary vortices in the midplane of wake of SC-I is weaker than that in the mid plane of the wake of SC-II.

The instantaneous variation of spanwise-averaged lifts on the TISC for the spacing of $H=0.5$ in the time range from 80 to 92 has been shown in Fig. 15. With respect to Fig. 15, the contours of spanwise vortices at six instants with a temporal interval 2 have been given in Fig. 16. The flow patterns for the case of $H=0.5$ are recognized as primary vortex pairing, splitting and enveloping patterns, as identified by Sumner et al.[2] The wake interference is intensive due to the small spacing. The two wakes emerge together, causing the vortex shedding frequency from both square cylinders identical. The impingement of the gap flow in the near-wake region of SC-I and the near-wake interference are reasons of the vortex pairing and splitting and enveloping of these primary vortices.

IV. CONCLUSIONS

This paper presents the simulation results of 3D flows around two identical square cylinders in staggered arrangements at a particular Reynolds number of 250 at zero incident angle, with the 45° angle between the incoming velocity vector and the line connecting the centers of the two cylinders. It was found that the secondary flow patterns are of
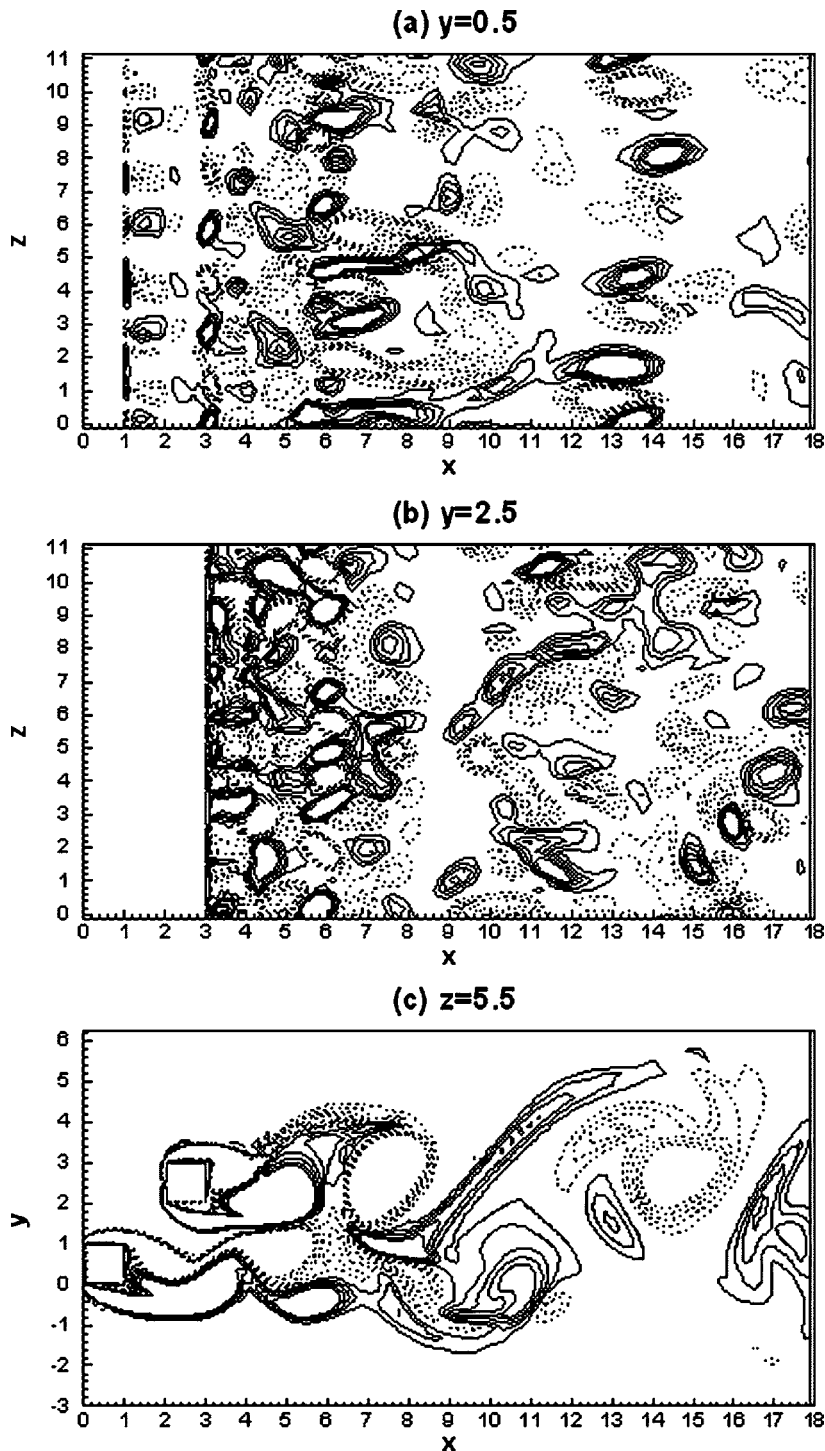
(a) y=0.5

(b) y=2.5

FIG. 13. Vorticity fields at the instant of $t=160$ for Re=250, $H=1$ (a) ω_y in the plane of $y=0.5$, (b) ω_y in the plane of $y=2.5$, and (c) ω_z in the plane of $z=5.5$. Note that the variation range and the increment of the vorticity component ω_y are given by $(\omega_{y\,min}, \omega_{y\,max}, \Delta\omega_y)=(-1,1,0.2)$, for ω_z it is assigned that $(\omega_{z\,min}, \omega_{z\,max}, \Delta\omega_z)=(-1,1,0.2)$, with the zero vorticity contour removed.

(c) z=5.5

mode B type in general, but due to the inherent characteristics of the TISC flow, the spanwise wavelength may be different from the values observed in single square cylinder flow. The momentum of the gap flow transferred into the near wake of the upstream square cylinder not only can suppress the oscillation of the drag and lift but also can suppress the generation of the secondary organized structures in the near wake of the cylinder. The gap flow also presents a mechanism causing the drag on the upstream square cylinder less than that on the downstream square cylinder.

Since the vortex separation on square cylinders has fixed separation points, and the lift on the upstream square cylin-

der exhibits duplicated oscillating frequencies, the present numerical results indicate that it is the upwind square cylinder rather than the downstream one that pertains duplicated Strouhal numbers. This is different from visualization in the staggered circular cylinder flows,[2] where it was shown that the duplicated Strouhal numbers are relevant to the vortex shedding from the two shear layers of the downstream circular cylinder.

The wake interference can result in an evident mutually attracting effect between the two identical square cylinders particular when the longitudinal spacing ranges from 1.0 to 1.5. The intensive wake interference can also result in the
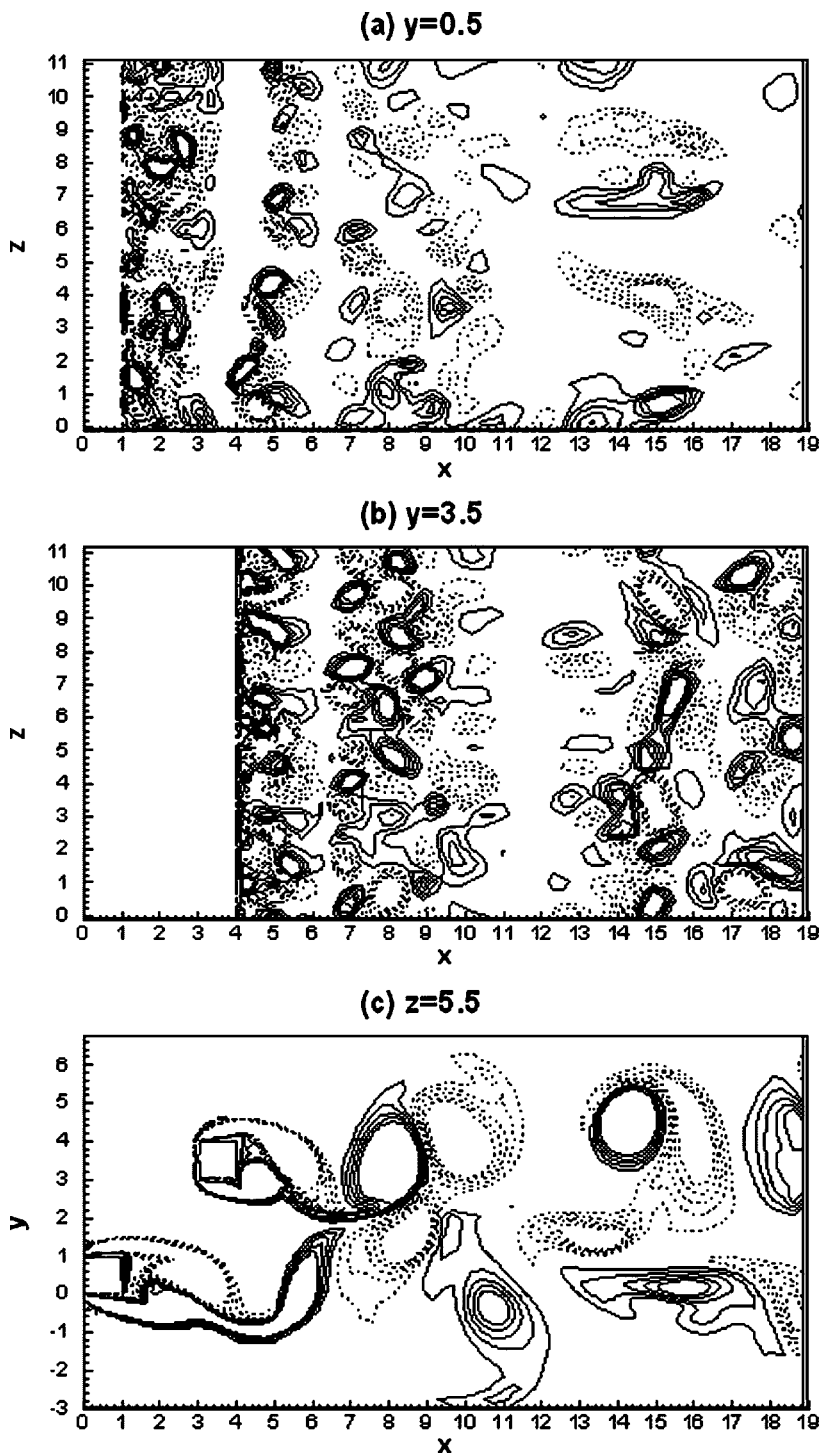
(a) y=0.5

(b) y=3.5

FIG. 14. Instantaneous vorticity fields for Re=250, $t=160$, and $H=2.0$: (a) ω_y at $y=0.5$; (b) ω_y at $y=3.5$; and (c) ω_z at $z=5.5$. Note that the vortices in parts (a) and (b) are labeled by $(\omega_{y\,min}, \omega_{y\,max}, \Delta\omega_y) = (-1, 1, .2)$, with those in part (c) labeled by $(\omega_{z\,min,z\,max}, \Delta\omega_z) = (-1, 1, 0.2)$, with the zero vorticity contour removed.

(c) z=5.5

change of the behavior of the primary vortex deformation, and hence lead to the secondary vortex enveloping. Such vortex enveloping in the secondary flows can significantly change the temporal evolution of the lift on both square cylinders.

Owing to the presence of the relatively strong secondary flows in the near wake of the downstream square cylinder, the spanwise correlation coefficients of the drag exhibit a wavy behavior in the spanwise direction, with the mean spanwise wavelength depending on the spacing of the two identical cylinders.
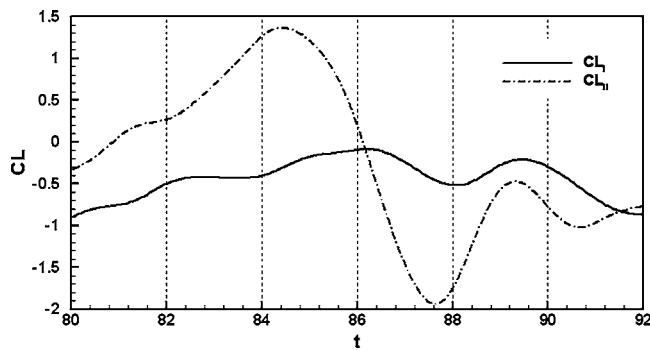

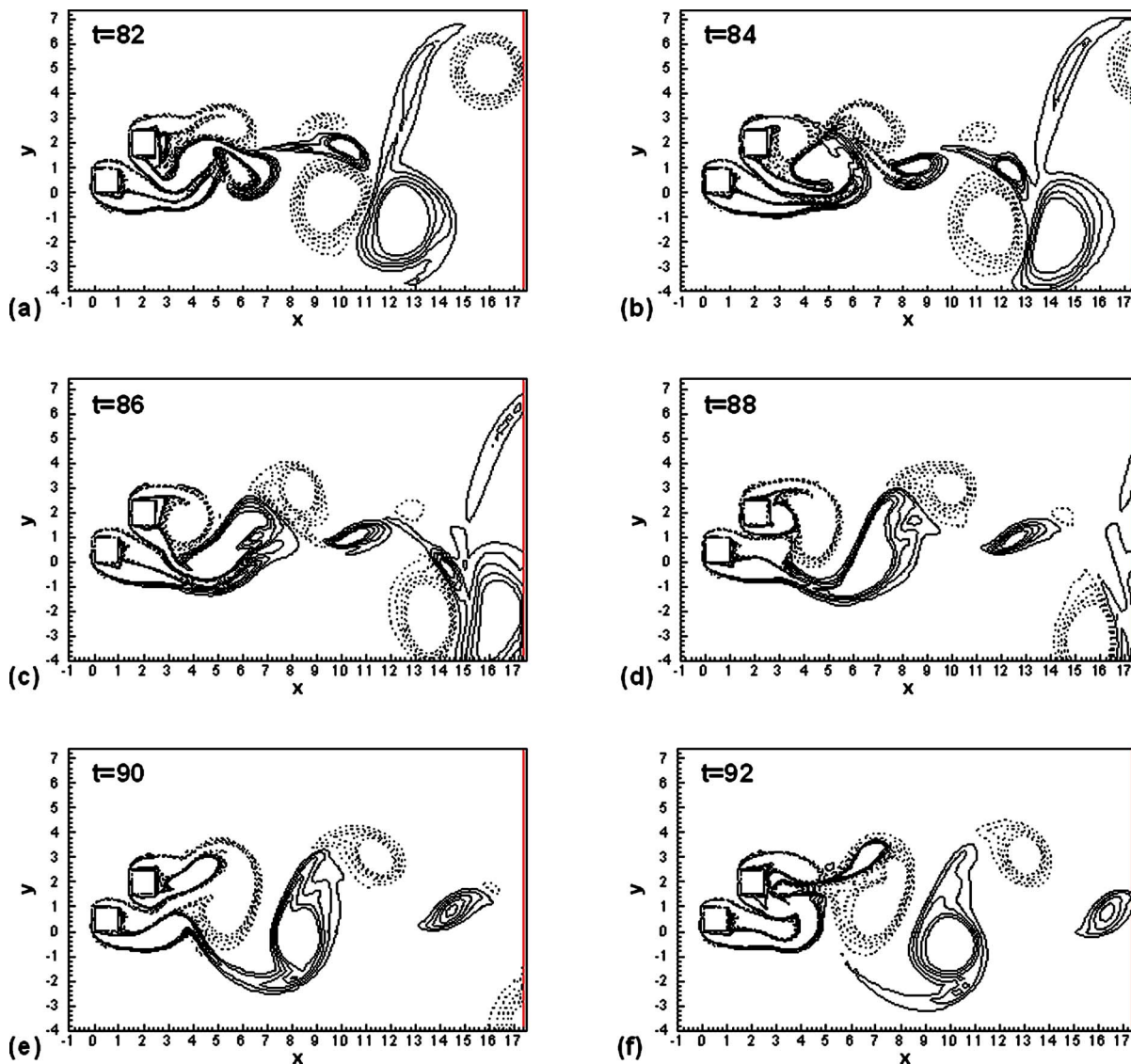FIG. 15. Instantaneous variation of lift for the two identical square cylinders when Re=250 and $H=0.5$.

FIG. 16. Vorticity fields in the near wake of the TISC for Re=250, H=0.5 in which parts (a)–(f) correspond to six different instants, the vorticity ω_z is assigned $(\omega_{z\,min}, \omega_{z\,max}, \Delta\omega_z) = (-1, 1, 0.2)$, with the zero vorticity contour removed.

ACKNOWLEDGMENTS

[1] I. T. S. Yu, Y. Li, T. W. Wong, W. Tam, A. T. Chan, J. H. W. Lee, D. Y. C. Leung, and T. Ho, "Evidence of airborne transmission of the severe acute respiratory syndrome virus," N. Engl. J. Med. **350**, 1731 (2004)

[2] D. Sumner, S. J. Price, and M. P. Paidoussis, "Flow-pattern identification for two staggered circular cylinders in cross- flow," J. Fluid Mech. **411**, 263 (2000).

[3] M. M. Zdravkovich, "Aerodynamics of two parallel circular cylinders of finite height at simulated high Reynolds numbers," J. Wind. Eng. Ind. Aerodyn. **6**, 59 (1980).

[4] M. M. Zdravkovich, "Interference between two circular cylinders forming a cross," J. Fluid Mech. **128**, 231 (1983).

[5] M. M. Zdravkovich, "Flow induced oscillations of two interference circular cylinders," J. Sound Vib. **104**, 511 (1985).

[6] M. M. Zdravkovich, "Review of interference-induced oscillations in flow past two parallel circular cylinders in various arrangements," J. Wind. Eng. Ind. Aerodyn. **28**, 183 (1988).

[7] P. T. Y. Wong, N. W. M. Ko, and A. Y. W. Chiu, "Flow characteristics around two parallel adjacent square cylinders of different sizes," J. Wind. Eng. Ind. Aerodyn. **54–55**, 263 (1995).

[8] H. J. Zhang and Y. Zhou, "Effect of unequal cylinder spacing on vortex streets behind three side-by-side cylinders," Phys. Fluids **13**, 3675 (2001).

[9] Md. Mahbub Alam, M. Moriya, and H. Sakamoto, "Aerodynamic characteristics of two side-by-side circular cylinders and application of wavelet analysis on the switching phenomenon," J. Fluids Struct. **18**, 325 (2003).

[10] S. C. Luo, L. L. Li, and D. A. Shah, "Aerodynamic stability of the downstream of two tandem square-section cylinders," J. Wind. Eng. Ind. Aerodyn. **79**, 79 (1999).

[11] A. Sohankar, C. Norberg, and L. Davidson, "Simulation of three-dimensional flow around a square cylinder at moderate Reynolds numbers," Phys. Fluids **11**, 288 (1999).

[12] A. K. Saha, G. Biswas, and K. Muralidhar, "Three-dimensional study of flow past a square cylinder at low Reynolds numbers," Int. J. Heat Fluid Flow **24**, 54 (2003).

[13] I. Olanski, "A simple boundary condition for unbounded flows," J. Comput. Phys. **21**, 251 (1976).

[14] D. L. Brown, R. Cortez, and M. L. Minion, "Accurate projection methods for the incompressible Navier-Stokes equations," J. Comput. Phys. **168**, 464 (2001).

[15] T. J. Baker, "Potential flow calculation by the approximate factorization

method," J. Comput. Phys. **42**, 1 (1981).

[16] H. Von Der Vorst, "BiCGSTAB: A fast and smoothly converging variant of BICG for the solution of non-symmetric linear system," SIAM (Soc. Ind. Appl. Math.) J. Sci. Stat. Comput. **13**, 631 (1992).

[17] H. X. Yang, Z. J. Zhu, and J. Gilleard, "Numerical simulation of thermal fluid instability between two horizontal parallel plates," Int. J. Heat Mass Transfer **44**, 1485 (2001).

[18] M. Pennacchio and V. Simoncini, "Efficient algebraic solution of reaction-diffusion system for cardiac excitation process," J. Comput. Appl. Math. **145**, 49 (2002).

[19] Y. H. Yang and Z. J. Zhu, "Exploring super-critical properties of secondary flows of natural convection in inclined channels," Int. J. Heat Mass Transfer **47**, 1217 (2004).

[20] A. Okajima, "Strouhal number of rectangular cylinders," J. Fluid Mech. **123**, 379 (1982).

[21] Z. J. Zhu and H. X. Yang, "Discrete Hilbert transformation and its application to estimate the wind speed in Hong Kong," J. Wind. Eng. Ind. Aerodyn. **90**, 9 (2002).

[22] Z. J. Zhu, "Numerical simulation of 3D viscous laminar flow around two square cylinders in closely staggered arrangement," Acta Mech. Sin. **34**, 425 (2002) (in Chinese).

[23] C. H. K. Williamson, "Vortex dynamics in the cylinder wake," Annu. Rev. Fluid Mech. **28**, 477 (1996).

[24] S. C. Luo, Y. T. Chew, and Y. T. Ng, "Characteristics of square cylinder wake transition flows," Phys. Fluids **15**, 2549 (2003).